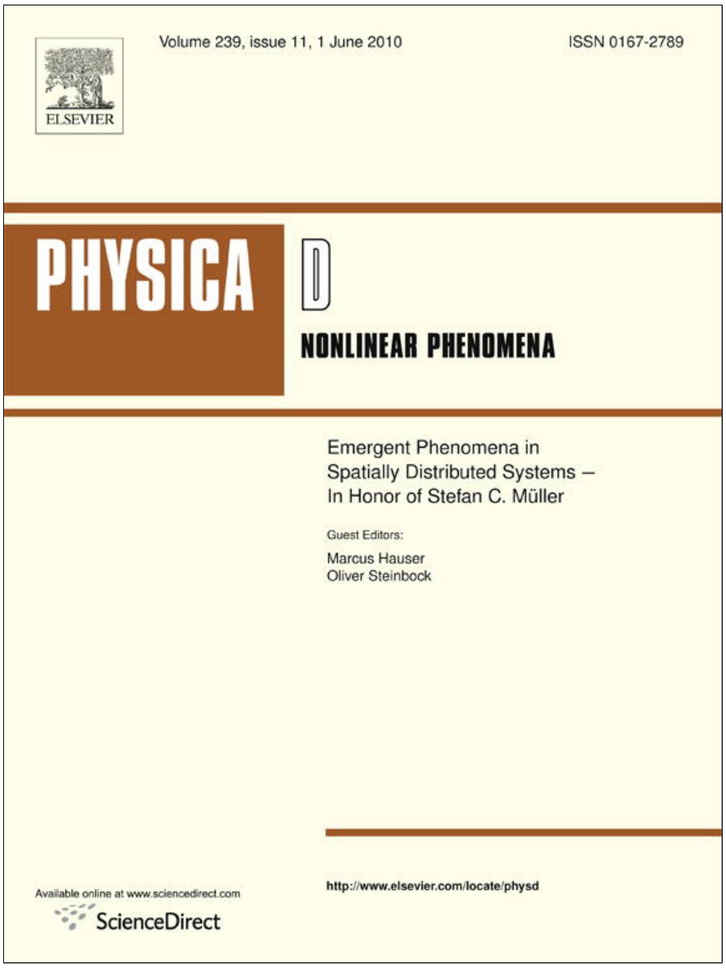

Volume 239, issue 11, 1 June 2010
ISSN 0167-2789

PHYSICA D
NONLINEAR PHENOMENA

Emergent Phenomena in
Spatially Distributed Systems –
In Honor of Stefan C. Müller

Guest Editors:
Marcus Hauser
Oliver Steinbock

http://www.elsevier.com/locate/physd

Physica D 239 (2010) 791–796

Contents lists available at ScienceDirect

Physica D

journal homepage: www.elsevier.com/locate/physd

Autocatalytic reaction dynamics in systems crowded by catalytic obstacles

Carlos Echeverria [a,b], Raymond Kapral [a,*]

[a] Chemical Physics Theory Group, Department of Chemistry, University of Toronto, Toronto, ON, M5S 3H6, Canada
[b] Laboratorio de Física Aplicada y Computacional, Universidad Nacional Experimental del Táchira, San Cristóbal 5001, Venezuela

ARTICLE INFO

Article history:
Available online 16 June 2009

Keywords:
Autocatalytic reactions
Crowded systems
Mesoscopic simulations

ABSTRACT

Reaction and diffusion dynamics in systems crowded by catalytic obstacles are investigated using a particle-based mesoscopic simulation method. The focus of the work is on effects of correlations induced by the presence of the catalytic obstacles and solvent collective modes. As an example, a system is considered where the reaction $A + C \rightarrow B + C$ takes place on the surfaces of the C catalytic obstacles, while the autocatalytic reaction $A + B \rightarrow 2A$ occurs in the bulk of the solution. It is shown that mean-field, mass-action rate laws break down and fail to describe the reaction dynamics for large volume fractions of obstacles. The influence of hydrodynamics on the reaction and diffusion dynamics is also studied.

1. Introduction

Reaction and diffusion dynamics in crowded systems is very different from that in simple solutions. Biological cells are prime examples of systems with crowded environments and the effects of crowding on processes such as protein conformational dynamics, aggregation and diffusion are topics of considerable interest [1–3]. Crowding also affects the dynamics of small molecules, although the effects are not as large as that for macromolecules [4]. In biological systems the crowding agents are microtubules and filaments, various organelles and other macromolecular species. Often the crowding agents are modeled by random arrays of spherical obstacles. The problem is then similar to the study of the dynamics in dense suspensions of colloidal particles. If reactions can occur on the surfaces of crowding agents then the problem is analogous to that of reaction dynamics for a random suspension of catalytic particles.

Smoluchowski's solution [5,6] of the diffusion equation for a single spherical catalytic particle[1] has provided the basis for much subsequent work on diffusion-influenced reaction dynamics. The generalization of this problem to reaction dynamics on dense arrays of reactive particles introduces new features to the reaction–diffusion kinetics. In particular, both the rate constant and diffusion coefficient depend on the volume fraction of the reactive particles in nontrivial ways. The theoretical treatments of this problem require that the long range nature of the diffusive coupling among the reactive obstacles be properly taken into account [9–11].

Most of the theoretical and simulation studies of reaction dynamics among a random distribution of catalytic obstacles have dealt with the simple situation where chemical species diffuse in solution and only react on contact with the catalytic particles. Here we study the situation where nonlinear autocatalytic reactions occur in the bulk of the solution, as well as reactions on the surfaces of the catalytic particles. Because of the discrete nature of the distribution of the catalytic particles and the perturbation of the species density fields that occur in their vicinity, the applicability of mean-field descriptions of the system is subject to question.

In Section 2 we present a general mesoscopic framework for simulating the dynamics of such systems. The method combines reactive multiparticle collision dynamics [12,13] for reactions occurring in the bulk of the solution with an event-driven reactive and nonreactive dynamics for the collisions between the catalytic obstacles and solution species [14,15]. As an example of the implementation of the method, Section 3 considers a system where the reaction $A + C \rightarrow B + C$ occurs on the surfaces of the obstacles and the autocatalytic reaction $A + B \rightarrow 2A$ occurs in the bulk of the solution. The nature of the reaction dynamics is studied as function of the obstacle density and size for various reaction rate regimes. The conclusions of the study are given in Section 4.

2. Reactive multiparticle collision dynamics

We consider a system comprising a large number of particles undergoing reactive dynamics. Specifically, we consider a three-dimensional system with volume $\mathcal{V}$ containing N_ℓ point particles

---

* Corresponding author. Tel.: +1 416 978 6106.
E-mail address: rkapral@gatto.chem.utoronto.ca (R. Kapral).

[1] A radiation boundary condition which allows for partial reflection and accounts for the presence of a diffusive boundary layer in the vicinity of the catalyst has also been used in such studies [7,8].

0167-2789/$ – see front matter © 2009 Elsevier B.V. All rights reserved.
doi:10.1016/j.physd.2009.06.005

of species ℓ with mass m, where the total number of particles is $N = \sum_\ell N_\ell$. The system may also contain N_C stationary catalytic obstacles C.

Multiparticle collision (MPC) dynamics [16–19], adapted to include chemical reactions [12,13], is used to simulate the time evolution of the system. In this mesoscopic description, particles with continuous positions and velocities free stream between multiparticle collision events that occur at discrete times τ. To carry out collisions, the volume $\mathcal{V}$ is divided into N_{cell} cubic cells of volume V_{cell}, where $\mathcal{V} = N_{cell} V_{cell}$. Each cell is labelled by an index ξ. Suppose that there are N_ℓ^ξ particles of species ℓ in cell ξ, giving a total number of $N_\xi = \sum_\ell N_\ell^\xi$ particles in the cell. Nonreactive collisions are carried out as follows: At every time τ each cell is assigned at random a rotation operator $\widehat{\omega}_\xi$, chosen from some set of rotation operators. If N_ξ is the instantaneous number of all particles in cell ξ, the center of mass velocity in the cell is $\mathbf{V}_\xi = N_\xi^{-1} \sum_{i=1}^{N_\xi} \mathbf{v}_i$ where $\mathbf{v}_i$ is the velocity of particle i. In MPC dynamics the post-collision velocity is given by $\mathbf{v}_i' = \mathbf{V}_\xi + \widehat{\omega}_\xi(\mathbf{v}_i - \mathbf{V}_\xi)$. This collision rule can be generalized to multi-component systems [14]. If $\ell_i \in \{1, 2, \ldots, s\}$ denotes the species label of particle i, then we may write the collision rule as

$$\mathbf{v}_i' = \mathbf{V}_\xi + \widehat{\omega}_\xi(\mathbf{V}_\xi^{\ell_i} - \mathbf{V}_\xi) + \widehat{\omega}_\xi^{\ell_i}\widehat{\omega}_\xi(\mathbf{v}_i - \mathbf{V}_\xi^{\ell_i}) \tag{1}$$

where $\mathbf{V}_\xi^{\ell_i}$ is the center of mass velocity of particles of species ℓ_i in cell ξ and $\widehat{\omega}_\xi$ and $\widehat{\omega}_\xi^{\ell_i}$ are again randomly chosen rotation operators. At each collision update $\widehat{\omega}_\xi$ acts on all particles in cell ξ and then $\widehat{\omega}_\xi^{\ell_i}$ acts on the subsets of particles of species ℓ_i in ξ. This collision rule conserves mass, momentum and energy and preserves phase space volumes.

We suppose that molecules in the bulk of the solution may also undergo chemical reactions of the form,

$$R_\mu : \sum_{\ell=1}^{s} \nu_\ell^\mu X_\ell \xrightarrow{k_\mu} \sum_{\ell=1}^{s} \overline{\nu}_\ell^\mu X_\ell, \tag{2}$$

where X_ℓ, $(\ell = 1, \ldots, s)$ are the s chemical species and ν_ℓ^μ and $\overline{\nu}_\ell^\mu$ are the stoichiometric coefficients for reaction R_μ. Reactive collisions occur in the MPC cells by stochastic rules as follows: The probability that a reaction R_μ will occur in a cell ξ with volume V_{cell} in $(t, t + \mathrm{d}t)$ is $k_\mu(V_{cell}) h_\mu^\xi \mathrm{d}t \equiv a_\mu^\xi \mathrm{d}t$ [12]. The factor a_μ^ξ for a randomly chosen reaction R_μ in cell ξ is given by

$$a_\mu^\xi = k_\mu(V_{cell}) \prod_{\ell=1}^{s} \frac{N_\ell^\xi!}{(N_\ell^\xi - \nu_\ell^\mu)!} \equiv k_\mu(V_{cell}) h_\mu^\xi, \tag{3}$$

where the notation $k_\mu(V_{cell})$ indicates that the rate constants have been scaled to account for the cell volume V_{cell}, and h_μ^ξ is a combinatorial factor that accounts for the number of different ways the reaction can occur in the cell. In reactive multiparticle collision (RMPC) dynamics, reactive collisions occur at discrete time intervals τ, and the probability that in the time interval τ the reaction R_μ will occur first, followed by any other events, is of interest and is given by

$$p_\mu^\xi(\mathbf{N}^\xi, \tau) = \frac{a_\mu^\xi}{a_0^\xi}(1 - \mathrm{e}^{-a_0^\xi \tau}), \tag{4}$$

where $\mathbf{N}^\xi$ is the vector of species populations in the cell.

If catalytic obstacles are present, then chemical reactions that convert species X_ℓ to $X_{\ell'}$ for specific ℓ and ℓ',

$$R_\mu : X_\ell + C \xrightarrow{k_\mu} X_{\ell'} + C, \tag{5}$$

take place on the surfaces of the obstacles. The volume fraction of obstacles is $\phi_C = N_C V_C / \mathcal{V}$, where V_C is the volume of an obstacle. In such reactions, particles of species X_ℓ encounter the catalytic particle and on encounter react to form product with probability p_μ [14].

3. Reaction dynamics with catalytic obstacles

The presence of a large number of catalytic sites can lead to cooperative effects that modify mass-action chemical rate laws and rate constants. There is a large literature that deals with such effects for simple catalytic reactions, using both theoretical and simulation treatments of the problem [20]. Most studies focus on the catalytic reactive event, with particles simply diffusing among the obstacles between reactive events. Here we study a situation where, in addition to reactive events on the surfaces of the catalysts, an autocatalytic reaction occurs in the bulk of the solution.

More specifically, we consider a system comprising a solution of reactive species $\ell = \{A, B\}$ and stationary, nearly randomly-distributed, cylindrical catalytic obstacles C with radius σ_C and height h. The following chemical reactions take place:

$$R_1 : A + C \xrightarrow{k_1} B + C \tag{6}$$

$$R_2 : A + B \xrightarrow{k_2} 2A. \tag{7}$$

Reaction R_1 occurs on the surfaces of the catalytic obstacles, while reaction R_2 occurs in the bulk of the solution.

3.1. *Single catalytic obstacle*

The presence of catalytic obstacles in the systems leads to concentration gradients in the obstacle vicinities which influence the reaction dynamics. We consider first a single catalytic particle with radius $\sigma_C = 10$ in the center of the system. The particle density fields in the vicinity of the catalyst are shown in Fig. 1 for two values of the k_2 reaction rate constant. Collisions of A with catalyst yield species B. Subsequently, B freely diffuses for a time that depends on the value of k_2, since this rate constant determines the rate at which B molecules will be transformed back to A by the reaction $A + B \rightarrow 2A$ in the solution. As the value of k_2 decreases, the B molecules will diffuse farther from the catalytic obstacle before they react in the bulk to form A. Thus, the interfacial zone around the catalyst increases with decreasing k_2 as seen in the figure.

The quantitative nature of the B density field in the vicinity of the catalytic obstacle can be determined from the radial function distribution of B with respect to center of the cylinder, $g_c^B(r)$, where $r = |\mathbf{r}_B - \mathbf{r}_C|$. This distribution function is seen in Fig. 2 which plots $g_c^B(r)$ for the same two values of k_2 as in Fig. 1. As expected, the B density field penetrates farther into the bulk of the solution as k_2 decreases since the reaction $A + B \rightarrow 2A$ that consumes B occurs at a slower rate. The existence of these nonequilibrium density profiles in the vicinity of the catalytic cylinder can lead to correlations among catalytic obstacles and play an important role in the reaction dynamics.

3.2. *Random distribution of catalytic obstacles*

When systems with random distributions of catalytic obstacles with high volume fraction are considered, cooperative effects arising from the diffusion fields perturbed by the presence of obstacles can modify diffusion and reaction rates. In particular, the concentration gradient in the vicinity of a single catalytic obstacle, which was discussed above, will interact with those from other obstacles in the system, and lead to correlated effects on the reaction–diffusion dynamics. In order to assess the importance of such correlations it is instructive to first consider a simple mean-field description of the system.

3.2.1. *Mean-field description*

If the catalytic obstacles were homogeneously distributed in the system and treated on the same footing as the A and B species, the mean-field, mass-action rate law for the system would be

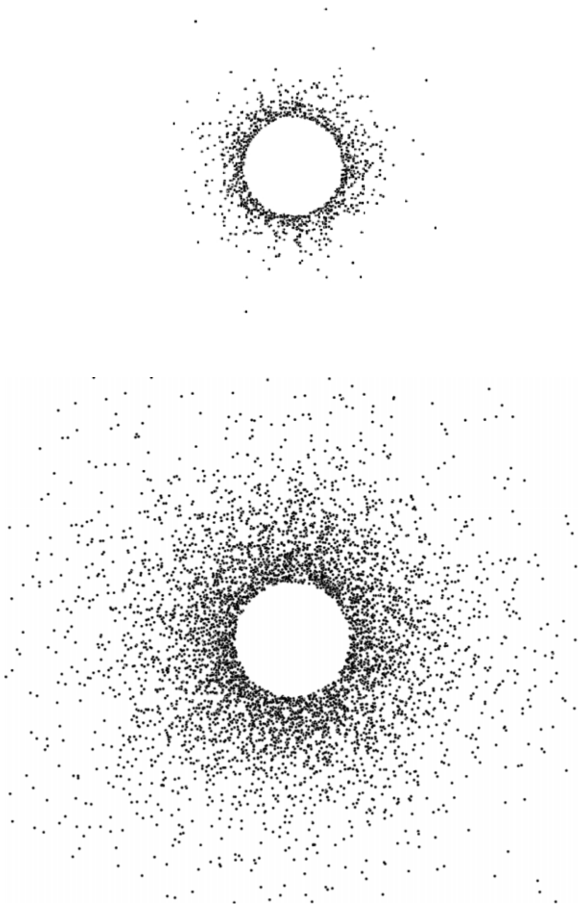

Fig. 1. Snapshots of the steady state B particle density field in the vicinity of the catalytic obstacle for a system with $\mathcal{V} = 100 \times 100 \times 1$, $T = 1/3$, $p_1 = 0.1$, $k_2 = 0.005$ (top) and $k_2 = 0.0005$ (bottom). The total density is $n = 10$. The top view of the catalytic cylinder is shown as an open circle.

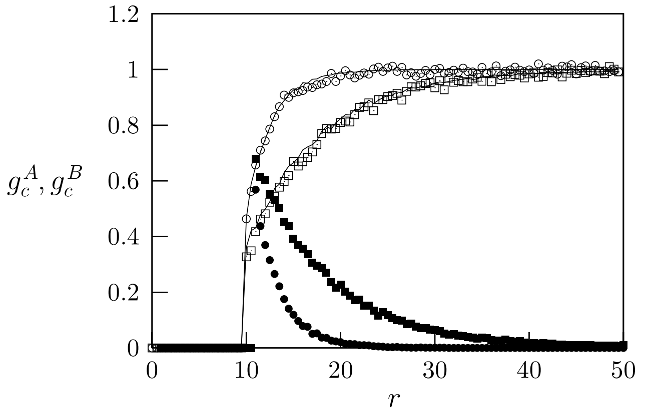

Fig. 2. B particle (filled symbols) and A particle (open symbols) radial distribution functions for the same conditions as in Fig. 1. Circles, $k_2 = 0.005$; squares, $k_2 = 0.0005$.

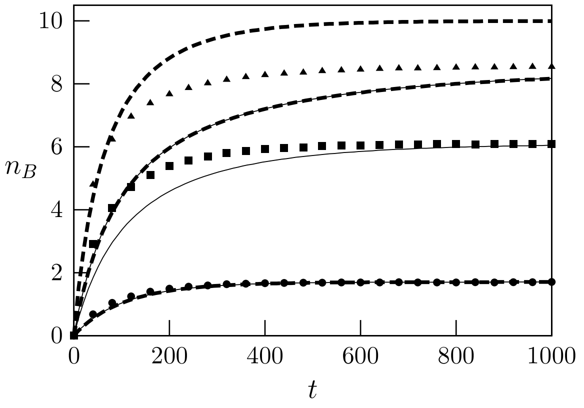

Fig. 3. The concentration $n_B(t)$ versus t. Parameter values: $p_1 = 0.1$, $k_2 = 0.001$ and $\sigma_C = 1$ for several values of the volume fraction: $\phi_C = 0.02$ (circles), 0.1 (squares) and 0.2 (triangles). The dashed lines are plots of Eq. (9) using k_1 determined from small volume fraction data. The lowest dashed curve coincides with the simulation data for $\phi_C = 0.02$ (circles), while the middle and top dashed curves should be compared with the data represented by squares and triangles, respectively. The solid lines are plots of Eq. (9) using k_1 using $n_B^*(\phi_C)$. The lowest solid line for $\phi_C = 0.02$ coincides with both the simulation data (circles) and the corresponding dashed line. The middle and top solid lines should be compared with data represented by squares and triangles, respectively. Fortuitously, the dashed line for $\phi_C = 0.1$ and the solid line for $\phi_C = 0.2$ are identical for the given parameter values.

$$\frac{\mathrm{d}n_B(t)}{\mathrm{d}t} = (n - n_B(t))(k_1 n_C - k_2 n_B(t)), \tag{8}$$

where the sum of the A and B particle densities is constant, $n_A(t) + n_B(t) = n = \text{const}$ and n_C is the constant number density of catalytic particles. We see that this system of equations admits two steady state solutions, $n_B^* = n$ and $n_B^* = k_1 n_C / k_2$. If $k_1 n_C < k_2 n$, $n_B^* = n$ is unstable and $n_B^* = k_1 n_C / k_2$ is stable. For the opposite inequality the stability is reversed. We focus on situations where $k_1 n_C < k_2 n$ and the relevant stable solution is $n_B^* = k_1 n_C / k_2$. In this case the time evolution of $n_B(t)$ is given by

$$n_B(t) = n\frac{(1 - \mathrm{e}^{\lambda t})}{(\gamma - \mathrm{e}^{\lambda t})}, \tag{9}$$

for $n_B(0) = 0$, where $\lambda = k_1 n_C - k_2 n$ and $\gamma = k_2 n / (k_1 n_C)$. The mean-field description assumes that species are completely mixed and cannot capture effects due to concentration inhomogeneities or correlations arising from the interactions among catalytic obstacles.

3.2.2. Simulation results

The full reaction–diffusion dynamics in the presence of an arbitrary number of catalytic obstacles can be simulated using reactive multiparticle collision dynamics. As described elsewhere [12], on long time scales for a well mixed system, this mesoscopic dynamics reduces to the mean-field, mass-action equations of chemical kinetics.

The simulations presented in this paper were carried out on systems with multiparticle collision cells of unit volume, $V_{cell} = 1$. The $\widehat{\omega}_\xi$ operators in the MPC dynamics were taken to describe rotations by $\alpha = \pm\pi/2$ about randomly chosen axes. The catalytic cylinder radius σ_C and volume fraction $\phi_C = N_C V_C / \mathcal{V}$, with $V_C = \pi\, \sigma_C^2\, h$, were varied. In systems with many obstacles, the obstacles were randomly placed in the volume, ensuring that there were no overlaps among the obstacles. When A or B particles collide with an obstacle MPC dynamics is not used, instead they undergo bounce-back collisions where their velocities change sign. The A particles additionally change to B with probability p_1 in such collisions. The total mean density of species A and B, $n_A + n_B = n$ was taken to be $n = 10$. The temperature in reduced units ($m = 1, V_{cell} = 1, \tau = 1$) was $T = 1/3$. Thus, a particle moving with a velocity corresponding to the mean thermal velocity will travel on average a distance of one cell between multiparticle collisions. For parameter regimes where the particles travel on average a small fraction of a cell, random multiparticle collision grid shifting can be introduced to restore Galilean invariance [21].

In our mesoscopic model, A particles impinge on the catalyst and react with probability p_1 to form B. Thus, the full rate for the reaction of A particles with the catalytic cylinder, k_1, contains contributions from the collision rate constant $k_1^{(0)} = p_1 Z$, where Z

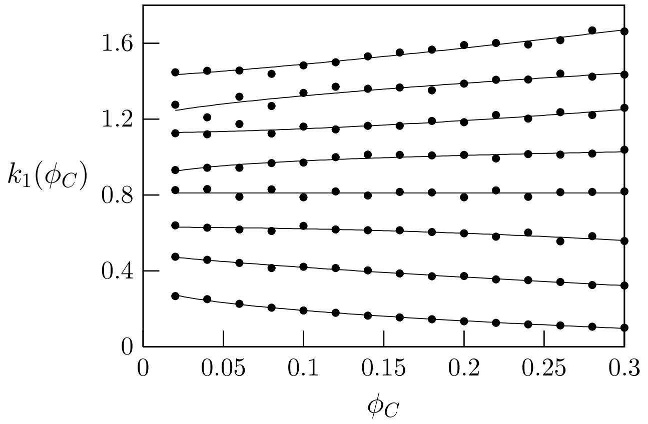

Fig. 4. The effective concentration-dependent $k_1(\phi_C)$ versus ϕ_C for several values of σ_C. Parameter values: $p_1 = 0.1$ and $k_2 = 0.001$. From bottom to top, the obstacle radius σ_C increases from $\sigma_C = 1$ to $\sigma_C = 8$ in units of 1. The fits are simply guides to the eye.

is the collision frequency, and the diffusion rate constant k_1^D that accounts for the diffusion of A particles to the reactive boundary layer around the catalytic particle [8,14]. The rate constant k_1 can be extracted from the simulation data for small volume fractions where each cylinder acts independently.

The validity of the mean-field description was tested by comparison of the time evolution of the B density given by Eq. (9) with the simulation results. The value of k_1 used in this comparison was determined from simulations at very small volume fractions of the B steady state density using the mean-field relation $k_1 = n_B^* k_2/n_C$. If simple mass-action kinetics were valid, this value of the rate constant would describe the time evolution at other higher values of the catalyst density.

Comparisons of the mesoscopic simulations with mass-action kinetics are presented in Fig. 3 for a system containing catalytic obstacles of radius $\sigma_C = 1$ for several values of the volume fraction. The system initially contains only A particles so that $n_B(0) = 0$.

As anticipated, at small volume fractions where correlations are very small and the value of k_1 was determined from n_B^*, the mass-action rate law is in agreement with the simulation data, except at the shortest times where it is expected to break down. Note the agreement between the simulation data (circles) and the dashed line that passes through these data points. However, significant deviations are seen for higher volume fractions. For the value of $k_2 = 0.001$ used in these simulations the characteristic width w_B of the B density profile around a catalytic obstacle can be determined from the B radial distribution function and is $w_B \approx 5$. This width is comparable to or larger than the average distance between obstacles at the higher volume fractions. For the other volume fractions, $\phi_C = 0.1$ and $\phi_C = 0.2$, the mean-field curves (dashed lines) deviate significantly from the simulation data and correlations among the catalytic particles manifest themselves as a breakdown of the mean-field mass-action rate law.

An effective volume fraction dependent rate constant can be extracted from the simulation data using $k_1(\phi) = n_B^*(\phi_C)k_2/n_C$, where $n_B^*(\phi_C)$ is the simulation value at volume fraction ϕ_C. This effective rate constant is plotted in Fig. 4 versus ϕ_C for several

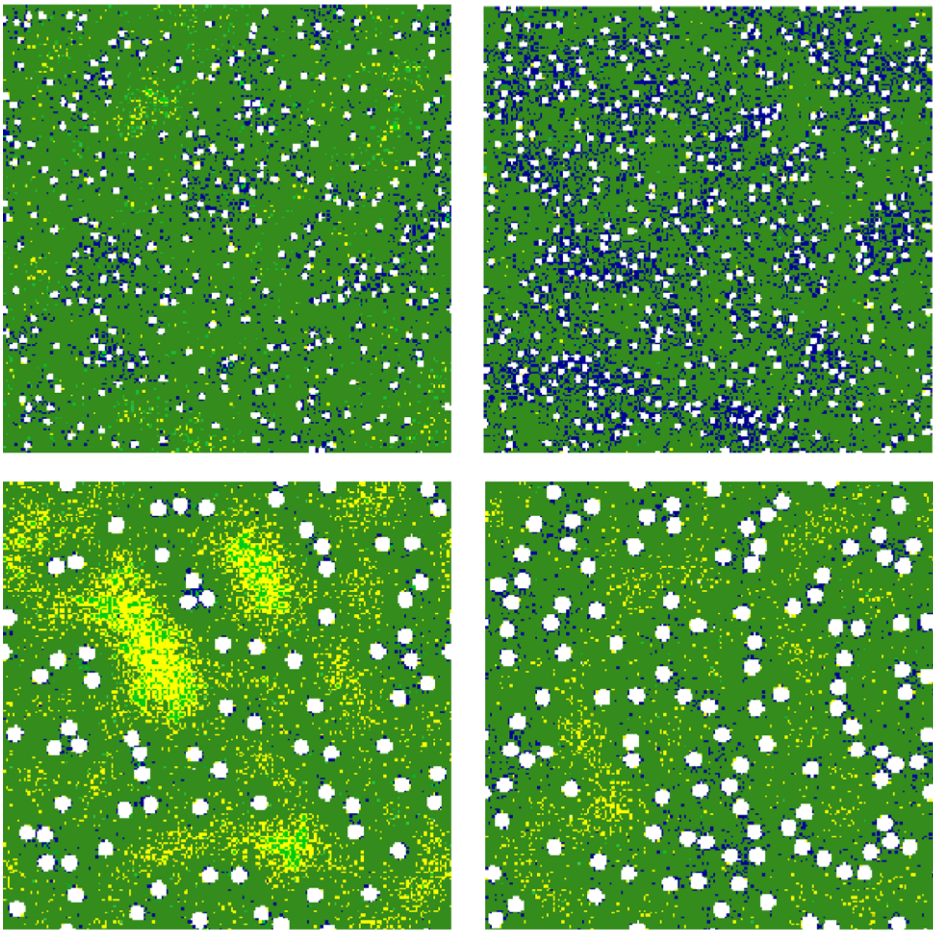

Fig. 5. Density fields of A and B particles and obstacle configurations for a system with $\mathcal{V} = 200 \times 200 \times 1$, $T = 1/3$, $k_1 = 0.1$, $k_2 = 0.001$, $\phi_C = 0.2$ (left column), $\phi_C = 0.3$ (right column), $\sigma_C = 2$ (top) and $\sigma_C = 4$ (bottom). Color code: B particles, blue, A particles, yellow and $A + B$ particles, green. (For interpretation of the references to colour in this figure legend, the reader is referred to the web version of this article.)

values of the catalyst radius σ_C. While the dependence on the volume fraction is not strong, there is an observable variation of k_1 with ϕ_C.

One may attempt to modify the mass-action rate law by using the ϕ_C-dependent rate constant $k_1(\phi_C)$ in place of the constant k_1. This comparison is also shown in Fig. 3 as the solid lines. Of course, now the asymptotic value n_B^* is given correctly but, except for the smallest volume fraction, this modification fails to describe the data for large volume fractions. Consequently, no simple modification of the mean-field equations can capture the effects of correlations induced by the presence of many catalytic obstacles.

Not only does the effective rate constant vary with ϕ_C but it also exhibits a nontrivial dependence on the obstacle radius. The increase of k_1 with increasing σ_C is expected in view of the larger collision frequency with the obstacles. However, we see that for small obstacle radii $k_1(\phi_C)$ decreases with ϕ_C, while for large σ_C it increases. These trends likely arise from competing effects of diffusion and reaction in the presence of obstacles. In our simulations the reaction probability on collision $p_1 = 0.1$ is small so that the majority of collisions with obstacles are simply bounce-back collisions as if the obstacles were inert. It is known that the effective rate constant for a single catalytic sphere in medium containing a dense suspension of noncatalytic obstacles leads to an effective rate constant that decreases with volume fraction, primarily as a result of a decrease in the effective diffusion coefficient [15]. It has also been shown by both theory [9,10] and simulation [14] that if random arrays of catalytic particles where the reaction probability is high are considered, then the effective reaction rate increases with volume fraction. For catalytic particles with large radii, even if the reaction probability is small, the production rate of B particles is large. One might then expect a cross-over to a $k_1(\phi_C)$ that increases with ϕ_C as observed in the simulations. To obtain a full quantitative description of these trends requires that one take into account the effects of the autocatalytic reaction in the bulk and the resulting complex correlations that arise from the catalytic obstacles in the presence of such bulk reactions.

In order to gain insight into the nature of the correlations arising from the presence of many obstacles, Fig. 5 shows the instantaneous particle density fields in the steady state regime along with the obstacle configurations for two different obstacle radii: $\sigma_C = 2$ (top) and $\sigma_C = 4$ (bottom). Results for two volume fractions are shown: $\phi_C = 0.2$ (left column) and $\phi_C = 0.3$ (right column). One can see that for $\phi_C = 0.2$ and $\sigma_C = 4$ large regions exist where there are predominantly A particles; these large A-rich regions are no longer present for $\phi_C = 0.3$, or for the smaller $\sigma_C = 2$ obstacle radius at either volume fraction. The rate of production of B particles on the surfaces of the catalytic obstacles depends on the total obstacle surface area, S_T. Given that surface area and volume of an obstacle are $S_C = 2\pi\sigma_C h$ and $V_C = \pi\sigma_C^2 h$, we have $S_T/\mathcal{V} = 2\phi_C/\sigma_C$. The smallest value of this surface area and smallest B particle production rate, occur when σ_C is large and ϕ_C is small, in accord with the results in Fig. 5.

The average structure of the B density field among the obstacles is seen more clearly by computing the B particle radial distribution function. This function is shown in Fig. 6 for the same parameters as in Fig. 5. For both large ($\sigma_C = 4$) and small ($\sigma_C = 2$) there is a build-up of B density around an obstacle as expected; however, for the smaller radius the asymptotic value is higher due to the larger total obstacle surface area. The density fields from different obstacles interact strongly, especially for the higher volume fraction, lower obstacle size case.

The insets in this figure show the obstacle radial distribution function. One can see that this distribution is not completely random; there are correlations at short distances that arise from obstacle clustering. The interplay among obstacle and solvent species density correlations give rise to domains where there are predominantly B particles (see especially the configuration for $\phi_C = 0.3$ and $\sigma_C = 2$ in the top right panel of Fig. 5). These strong correlations again lead to a breakdown of the mean-field description. σ_C

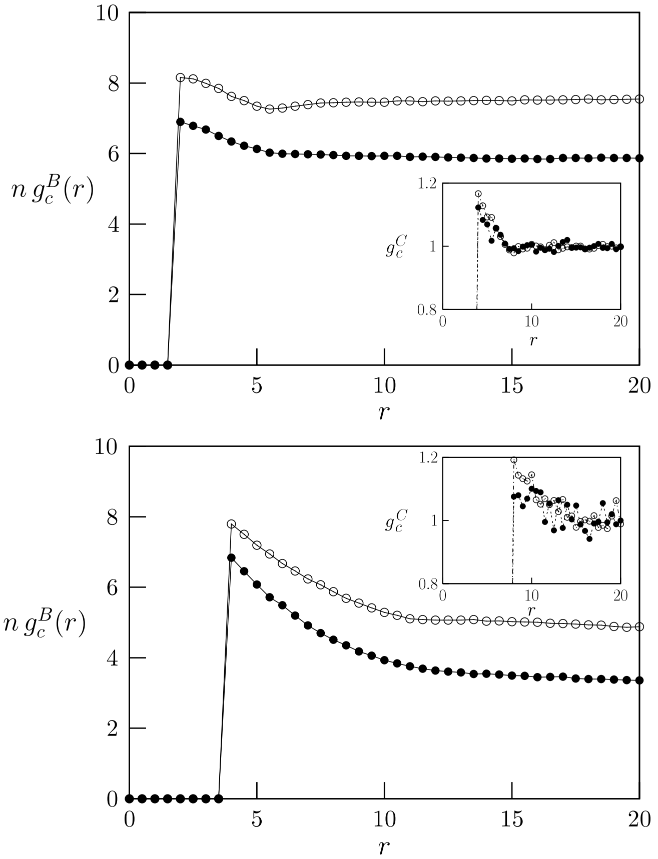

Fig. 6. The B particle radial distribution function for the same conditions as in Fig. 5. Open circles, $\phi_c = 0.3$; full circles, $\phi_C = 0.2$. Top, $\sigma_C = 2$; bottom, $\sigma_C = 4$. The insets in these figures show the obstacle radial distribution function.

3.2.3. *Effects of hydrodynamics*

The last issue we address is the role of hydrodynamics on the reaction–diffusion dynamics of this autocatalytic system. Our mesoscopic RMPC dynamics simulations conserve mass, momentum and energy, as does full molecular dynamics. Therefore, all hydrodynamic effects are automatically incorporated in the simulations. While there are no bulk fluid flows present and our reactions are thermoneutral, hydrodynamics can still influence the transport properties of the system and thus affect the dynamics and correlations that exist in the system. It is an easy matter to modify the dynamics in order to remove the correlations induced by hydrodynamic coupling to the conserved fluid modes [18,19]. One may simply replace the MPC dynamics by random sampling of the post-collision velocity from a Boltzmann distribution.

The effects of these hydrodynamic correlations are seen in Fig. 7 which plots n_B^* as function of the volume fraction ϕ_C, from full RMPC dynamics and dynamics without hydrodynamic coupling. Results are shown for $k_2 = 0.001$ and several values of σ_C. Other parameters are the same as those in Fig. 3. There are large differences in the values of n_B^* determined from dynamics with or without hydrodynamic effects. The discrepancies are especially great for the smallest obstacle radius where the larger number of obstacles give rise to perturbations of the solvent concentration fields. These results point to the importance of properly accounting

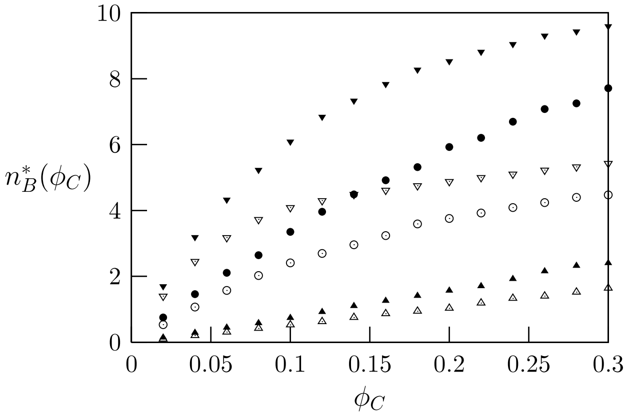

Fig. 7. Comparison of dynamics with (filled symbols) and without (symbols with central dot) hydrodynamics. The plot shows n_B^* versus ϕ_C. Parameter values: $p_1 = 0.1$, $k_2 = 0.001$ for several values of σ_C: $\sigma_C = 1$ (downward triangles), 2 (circles) and 8 (triangles).

for solvent dynamical modes in the reaction–diffusion dynamics of this system.

4. Conclusion

Theoretical descriptions of reaction–diffusion dynamics in heterogeneous media present technical challenges because of the need to account for dynamical correlations. Many systems of this type that are encountered in nature are complicated, both because of the nature and distribution of crowding obstacles and the complex chemistry that takes place in the system.

Molecular simulation provides a means to study these more complex situations. The hybrid reactive multiparticle collision dynamics scheme implemented in this paper provides one such route to the simulation of the dynamics of these systems. While the model reaction network studied in this paper is very simple, it does capture features which are expected to be generic for class systems of this type. In particular, it shows how autocatalytic reactions in the bulk of the solution can be combined with reactions on dense configurations of catalytic obstacles to yield kinetics that cannot be described by simple mean-field theory. Since the simulation method preserves many features of full molecular dynamics, hydrodynamic interactions and their effects on transport properties are accounted for in the simulations. These effects can play important roles in the dynamics. This is evident in Fig. 3 where strong deviations from mean-field mass-action kinetic are observed, and in Fig. 7 where the effects of coupling to conserved solvent modes are shown to influence the steady state B density.

The simulation scheme is easily adapted to describe more complex reaction networks and to obstacles with arbitrary geometries. Therefore, it may be used to investigate a variety of systems of chemical and biochemical interest where molecular crowding plays an important role.

Acknowledgments

This work was supported in part by a grant from the Natural Sciences and Engineering Research Council of Canada. One of the authors (C.E.) acknowledges support from Decanato de Investigación, Universidad Nacional Experimental del Táchira, San Cristóbal, Venezuela.

References

[1] T.C. Laurent, Biophys. Chem. 57 (1995) 7.
[2] S.P. Zimmerman, A.P. Minton, Annu. Rev. Biophys. Struct. 22 (1993) 27.
[3] A.P. Minton, J. Biol. Chem. 276 (2001) 10577.
[4] A.S. Verkman, TRENDS in Biochem. Sci. 27 (2002) 27.
[5] M. von Smoluchowski, Ann. Phys. 48 (1915) 1003; Phys. Z. 17 (1916) 557.
[6] M. von Smoluchowski, Z. Phys. Chem. 92 (1917) 129.
[7] F.C. Collins, G.E. Kimball, J. Colloid Sci. 4 (1949) 425.
[8] R. Kapral, Adv. Chem. Phys. 48 (1981) 71.
[9] B.U. Felderhof, J.M. Deutch, J. Chem. Phys. 64 (1976) 4551.
[10] J. Lebenhaft, R. Kapral, J. Stat. Phys. 20 (1979) 25.
[11] I.V. Gopich, A.M. Berezhkovskii, A. Szabo, J. Chem. Phys. 117 (2002) 2987.
[12] K. Rohlf, S. Fraser, R. Kapral, Comp. Phys. Comm. 179 (2008) 132.
[13] K. Tucci, R. Kapral, J. Phys. Chem. B 109 (2005) 21300.
[14] K. Tucci, R. Kapral, J. Chem. Phys. 120 (2004) 8262.
[15] C. Echeverria, K. Tucci, R. Kapral, J. Phys.: Condens. Matter 19 (2007) 065146.
[16] A. Malevanets, R. Kapral, J. Chem. Phys. 110 (1999) 8605.
[17] A. Malevanets, R. Kapral, J. Chem. Phys. 112 (2000) 7260.
[18] R. Kapral, Adv. Chem. Phys. 140 (2008) 89.
[19] G. Gompper, T. Ihle, D.M. Kroll, R.G. Winkler, Adv. Polym. Sci. 221 (2008) 1.
[20] D.F. Calif, J.M. Deutch, Annu. Rev. Phys. Chem. 34 (1983) 493.
[21] T. Ihle, D.M. Kroll, Phys. Rev. E 63 (2001) 020201.